Numerical study of solitary wave attenuation in a fragmented ice sheet

Philippe Guyenne[*]

Department of Mathematical Sciences, University of Delaware, Newark, Delaware 19716, USA

Emilian I. Părău

School of Mathematics, University of East Anglia, Norwich NR4 7TJ, United Kingdom

A numerical model for direct phase-resolved simulation of nonlinear ocean waves propagating through fragmented sea ice is proposed. In view are applications to wave propagation and attenuation across the marginal ice zone. This model solves the full equations for nonlinear potential flow coupled with a nonlinear thin-plate formulation for the ice cover. A key contribution is to modeling fragmented sea ice, which is accomplished by allowing the coefficient of flexural rigidity to vary spatially so that distributions of ice floes can be directly specified in the physical domain. Two-dimensional simulations are performed to examine the attenuation of solitary waves by scattering through an irregular array of ice floes. Two different measures based on the wave profile are used to quantify its attenuation over time for various floe configurations. Slow (near linear) or fast (exponential-like) decay is observed depending on such parameters as incident wave height, ice concentration, and ice fragmentation.

I. INTRODUCTION

The recurrent interactions between ocean waves and sea ice are a widespread feature of the polar regions and their impact on sea-ice dynamics and morphology has been increasingly recognized as evidenced by the surge of research activity during the past two decades. The rapid decline of summer ice extent that has occurred in the Arctic Ocean over recent years has certainly contributed to the renewed interest in this subject [1,2]. Global warming has been blamed for such a change because warmer temperatures reduce the ice cover and allow the exposed surface to absorb more solar energy, which in turn leads to more warming and ice melting. While there is no doubt that such a process (called ice-albedo feedback) has been a major factor in transforming the Arctic seascape, this has likely been aggravated by the action of ocean waves and their increased activity in recent decades [3]. By breaking up the sea ice, incident waves cause it to become more fragmented as typically occurring in the transitional region called the marginal ice zone (MIZ) between the open ocean and the pack-ice cover. This leads to an increased capacity for ocean waves to further penetrate and damage the ice cover.

While the problem of ocean waves interacting with sea ice has drawn attention for some time now, the vast majority of theoretical studies have used linear approximations of the governing equations. Based on linear potential-flow theory for the underlying fluid and linear plate theory for the floating ice, a boundary value problem is typically formulated in the frequency domain. Of particular interest is the description of wave attenuation through ice-covered seas. This direction of inquiry has produced abundant literature and has reached a high degree of sophistication spanning a variety of situations. For the MIZ, two different viewpoints have been adopted: (i) continuum models for waves propagating through an inhomogeneous ice cover described as a uniform material with effective properties including viscosity or viscoelasticity [4,5] and (ii) separate-floe models where the ice cover is composed of individual floes with possibly different characteristics [6–11]. Unlike

---

[*]guyenne@udel.edu

case (i), which includes dissipative processes, case (ii) focuses on wave attenuation by scattering through the heterogeneous ice field. Indeed, measurements from Wadhams *et al.* [12] provided evidence that wave scattering by ice floes is the dominant mechanism for energy attenuation in the MIZ. Theoretical predictions based on this mechanism typically give an exponential decay of linear waves with distance traveled through sea ice. A review on this body of work was written by Squire [13].

Ocean waves, however, are inherently nonlinear and, from the perspective of global warming, it is also expected that powerful storms with associated large waves will become more commonplace around the globe, with direct consequences on the sea ice. Two recent field studies made headlines by providing supporting evidence for this scenario: Thomson and Rogers [14] observed 5-m waves in the Arctic Beaufort Sea, while Kohout *et al.* [15] measured wave heights greater than 3 m in the Antarctic Southern Ocean. The latter study found that such large waves can travel hundreds of kilometers across the MIZ and they attenuate at a much slower (almost linear) pace than the commonly assumed exponential rate. This supports previous reports of intense waves-in-ice events that have highlighted limitations of the linear theory [16].

Despite some progress in recent years, the nonlinear theory is still in its infancy. Work has so far focused on the analysis and simulation of flexural-gravity waves in continuous uniform sea ice and has employed thin-plate theory (linear Euler-Bernoulli theory and nonlinear extensions) for the ice combined with nonlinear potential-flow theory for the fluid. Flexural-gravity waves are so called because their motion is subject to two restoring forces: gravity and elastic bending of the plate. Results include weakly nonlinear modeling in various asymptotic regimes as well as direct numerical simulation [17–20]. Plotnikov and Toland [21] proposed a thin-plate formulation with a conservative and nonlinear expression for the bending force, which has subsequently been used by other investigators [22–25]. Because no viscosity or other attenuating effects were considered in these nonlinear studies, the main objective was to characterize localized traveling waves such as those generated by a moving load on ice.

Numerical and theoretical work on nonlinear waves propagating in fragmented sea ice is even more scarce, and this largely remains an unexplored problem. The discrete element method, which models sea ice by densely packed particles, has been developed to simulate, e.g., pancake-ice dynamics under wave action [26], but linear approximations were used for the driving flow. Hegarty and Squire [27] examined the interaction of large-amplitude ocean waves with a compliant floating raft such as an ice floe and computed the perturbative solution up to second order via a boundary integral method. Doble and Bidlot [28] and Li *et al.* [29] simulated nonlinear wave propagation in the MIZ by using phase-averaged spectral models (WAM and WAVEWATCH III, respectively) combined with parametrizations that assume exponential decay due to sea ice. However, at the coarse grid sizes and large scales represented by such phase-averaged models, the MIZ is essentially viewed as a continuous ice cover.

In the present paper we propose a numerical model that allows for phase-resolved simulation of nonlinear ocean waves propagating through fragmented sea ice, with a focus on modeling the fragmented ice cover. As an extension of the high-order spectral method of Craig and Sulem [30], this model solves the full time-dependent equations for nonlinear potential flow and a key feature is that it can directly incorporate spatial distributions of ice floes. The ice cover is viewed as an elastic material according to the thin-plate formulation of Plotnikov and Toland [21], with an *ad hoc* modification to define its spatial dependence. Because emphasis is put on nonlinear wave effects, fragmented sea ice is represented in such a way that the overall approach is well suited to direct numerical simulation. Dissipative effects from, e.g., ice viscosity and floe-floe collisions are neglected. Our main goal is to emulate and investigate wave attenuation by scattering through an irregular array of ice floes, as it may occur in the MIZ, from a deterministic and nonlinear point of view. In this preliminary study, we only consider the two-dimensional finite-depth problem and prescribe solitary water waves as incident wave conditions.

Although solitary waves may not be of direct relevance to wave-ice interactions in the ocean, their use is compelling for a number of reasons.

(a) This paper is focused on nonlinear waves for which solitary waves are a well-known representative example.

(b) As described in the classical water wave problem, they may be viewed as a prototype for long swell waves, which are particularly energetic incident waves among the spectrum of wind-driven ocean waves and thus can propagate far into the ice field [15].

(c) They are also a good approximation for tsunamis for which there have been notable cases of interaction with floating ice. For example, part of the 2011 Tohoku tsunami traveled across the Pacific Ocean and caused large Manhattan-size icebergs to break off the Sulzberger Ice Shelf in Antarctica [31]. A landslide occurring on the shore of an ice-covered lake near Montréal (Canada) in April 2014 triggered a tsunami that damaged several seasonal residences and boathouses in an area extending over 500 m from the landslide debris location [32].

(d) Considering such long waves as solitary waves further justifies the use of our thin-plate model for the ice sheet. Indeed, a requirement for the thin-plate approximation to hold is that the wavelength be much longer than the plate thickness.

(e) Employing solitary waves is convenient from a practical point of view because their localized and progressive character makes it easy to identify and quantify their attenuation over time as they travel across the ice cover.

(f) Moreover, due to their localized character, undesirable wave reflection or transmission from the lateral boundaries of the computational domain is not a major concern. Otherwise, it would be necessary to address this issue if the waveform was spatially extended. Developing effective methods for nonreflecting boundary conditions in time-dependent numerical simulations of nonlinear waves is known to be a particularly challenging problem [33].

Because we consider the full nonlinear equations of this hydroelastic problem, care is taken to specify numerically exact solitary wave solutions to the water wave problem as incident wave conditions. Otherwise, the use of a weakly nonlinear long-wave approximation such as a Korteweg–de Vries (KdV) soliton or any other arbitrary pulse would likely promote wave radiation and overestimate the subsequent attenuation rate.

The remainder of this paper is organized as follows. Section II presents the mathematical formulation of this hydroelastic problem, including the model for fragmented sea ice. Section III shows numerical results on wave attenuation for various floe configurations. Two different measures of wave attenuation are discussed with respect to such parameters as incident wave height, ice concentration, and ice fragmentation.

II. MATHEMATICAL FORMULATION

A. Governing equations

We consider a two-dimensional fluid of uniform finite depth h lying beneath a continuous ice sheet. Dissipative effects are neglected in this problem. The fluid is assumed to be incompressible and inviscid and the flow to be irrotational. The ice sheet is modeled as a thin elastic plate according to the special Cosserat theory of hyperelastic shells in Cartesian coordinates (x, y), with the x axis being the bottom of the ice sheet at rest and the y axis directed vertically upward [21]. The vertical displacement of the ice is denoted by $y = \eta(x, t)$. The fluid velocity potential $\Phi(x, y, t)$ satisfies the Laplace equation

$$\nabla^2 \Phi = 0 \text{ for } x \in \mathbb{R}, \quad -h < y < \eta(x, t). \tag{1}$$

The nonlinear boundary conditions at $y = \eta(x, t)$ are the kinematic condition

$$\partial_t \eta + (\partial_x \Phi)(\partial_x \eta) = \partial_y \Phi \tag{2}$$

and the dynamic (or Bernoulli) condition

$$\partial_t \Phi + \frac{1}{2}|\boldsymbol{\nabla}\Phi|^2 + g\eta + \frac{\sigma}{\rho}\left(\partial_s^2 \kappa + \frac{1}{2}\kappa^3\right) = 0, \tag{3}$$

where κ is the mean curvature at any point of the fluid-ice interface and s is the arc length along this interface. In terms of η, the mean curvature is given by

$$\kappa = \frac{\partial_x^2 \eta}{[1 + (\partial_x \eta)^2]^{3/2}}$$

and so the nonlinear bending force exerted by the ice sheet onto the fluid surface reads

$$\partial_s^2 \kappa + \frac{1}{2}\kappa^3 = \frac{1}{\sqrt{1 + (\partial_x \eta)^2}}\partial_x \left[\frac{1}{\sqrt{1 + (\partial_x \eta)^2}}\partial_x \left(\frac{\partial_x^2 \eta}{[1 + (\partial_x \eta)^2]^{3/2}} \right) \right] + \frac{1}{2}\left(\frac{\partial_x^2 \eta}{[1 + (\partial_x \eta)^2]^{3/2}} \right)^3.$$

This system of equations is completed with the no-flux boundary condition at the rigid bottom, namely,

$$\partial_y \Phi = 0 \quad \text{at } y = -h. \tag{4}$$

In Eq. (3), the coefficient $g \simeq 9.8 \text{ m s}^{-2}$ is the acceleration due to gravity, $\rho \simeq 1025 \text{ kg m}^{-3}$ is the fluid density, and σ is the parameter of flexural rigidity for the ice sheet, as defined by

$$\sigma = \frac{E\ell^3}{12(1 - \nu^2)},$$

where $E \simeq 6 \text{ GPa}$ and $\nu \simeq 0.3$ denote Young's modulus and Poisson's ratio for the ice, respectively, and ℓ is its average thickness. The inertia of the thin elastic plate is neglected, so the plate acceleration term is not taken into account. We also assume that the elastic plate is not prestressed and neglect plate stretching. These assumptions are generally reasonable and even more so in the MIZ where the ice cover is especially compliant [34].

This formulation of the hydroelastic problem is both nonlinear and conservative in the sense that it conserves the total energy

$$H = \frac{1}{2}\int_{-\infty}^{\infty}\int_{-h}^{\eta}|\nabla\Phi|^2 dy\, dx + \frac{1}{2}\int_{-\infty}^{\infty}\left[g\eta^2 + \frac{\sigma}{\rho}\kappa^2\sqrt{1 + (\partial_x\eta)^2} \right]dx \tag{5}$$

and thus may be cast into Hamiltonian form as shown in the next section. The first integral in Eq. (5) represents kinetic energy, while the second integral represents potential energy due to gravity and elasticity.

B. Dirichlet-Neumann operator

Following Guyenne and Părău [22,24], we can reduce the dimensionality of the Laplace problem (1)–(4) by introducing $\xi(x,t) = \Phi(x,\eta(x,t),t)$, the trace of the velocity potential on $y = \eta(x,t)$, together with the Dirichlet-Neumann operator (DNO)

$$G(\eta)\xi = (-\partial_x\eta, 1)^\top \cdot \nabla\Phi|_{y=\eta},$$

which is the singular integral operator that takes Dirichlet data ξ on $y = \eta(x,t)$, solves the Laplace equation (1) for Φ subject to (4) and returns the corresponding Neumann data (i.e., the normal fluid velocity there) [35].

In terms of these boundary variables, the equations of motion (2) and (3) take the form

$$\partial_t\eta = G(\eta)\xi, \tag{6}$$

$$\partial_t\xi = -\frac{1}{2[1 + (\partial_x\eta)^2]}\{(\partial_x\xi)^2 - [G(\eta)\xi]^2 - 2(\partial_x\xi)(\partial_x\eta)G(\eta)\xi\} - g\eta - \frac{\sigma}{\rho}\left(\partial_s^2\kappa + \frac{1}{2}\kappa^3 \right). \tag{7}$$

This is a closed Hamiltonian system for the conjugate variables η and ξ, with the Hamiltonian corresponding to (5), which extends the well-known Zakharov Hamiltonian formulation for water waves [36] to flexural-gravity waves (i.e., ice-covered ocean waves) [37,38].

The dispersion relation for linear time-harmonic solutions is

$$c^2 = \left(\frac{g}{k} + \frac{\sigma k^3}{\rho} \right) \tanh(hk), \tag{8}$$

where c and k denote the phase speed and wave number, respectively. It can be shown that the phase speed $c(k)$ has a minimum c_{min} at $k = k_{min}$ for any choice of parameter values [18]. At this minimum, the phase speed and group speed are equal. In the long-wave limit $k \to 0$, $c(k)$ reduces to $c_0 = \sqrt{gh}$ as in the ice-free water wave problem.

Recall that this mathematical formulation is originally meant to describe a continuous ice sheet of infinite extent. However, as presented in Sec. II C, we will use it as a building block to model wave propagation in fragmented sea ice. A consequence of this modification is that the above Hamiltonian structure will be lost, meaning that the counterpart to (5) will no longer be a conserved quantity, but we will still be able to exploit the dynamical equations (6) and (7) that lend themselves well to numerical simulation due to their lower-dimensional form. For this purpose, Eqs. (6) and (7) are nondimensionalized using the characteristic scales $(\sigma/\rho g)^{1/4}$ and $(\sigma g^3/\rho)^{1/8}$ as unit length and unit speed, respectively, so that $g = 1$ and $\sigma/\rho = 1$ [20].

C. Model of fragmented sea ice

How can we directly specify a spatial distribution of ice floes and couple it to fluid motion in the nonlinear setting (6) and (7)? The synthesis procedure based on the superposition of wave fields as employed in previous linear studies is clearly not suitable here [13]. This is quite a nontrivial problem: Not only do we need to devise a local way of accommodating the ice-water boundary, but we also need to simulate a global pattern of ice floes that resembles the MIZ.

Our idea is to combine the continuum and piecewise points of view. By exploiting the fact that the dynamic boundary condition (7) is determined up to an interfacial pressure term, we may model the MIZ as a spatial distribution of icy and wet areas where the bending force is turned on and off, respectively. In other words, the coefficient of flexural rigidity may now be viewed as a spatial function $f(x)\sigma/\rho$ whose amplitude varies between 0 (open water) and σ/ρ (pack ice). The transition between the two phases should be made steep but smooth enough to clearly distinguish the individual floes while complying with the continuum character of the underlying formulation. Such a way of manipulating the pressure term (here the bending force) bears resemblance to the strategy adopted in previous numerical studies where a localized pressure distribution is applied on the free surface to reproduce various desired effects, e.g., by Longuet-Higgins and Cokelet [39] to simulate the breaking of surface gravity waves under wind action, by Clément [40] to specify an absorbing beach that dissipates outgoing waves at one end of the computational domain, and by Guyenne and Părău [22,23] to compute flexural-gravity waves resulting from a moving load on ice. This is also similar to the work of Williams and Squire [41], who described a continuous ice sheet with variable topography by allowing its properties such as flexural rigidity to exhibit a spatial dependence, although these authors did not consider the case of an ice-water transition in their study.

Of course, this continuum wave-ice model is not supposed to be able to capture all the complex phenomena that may occur at such a boundary. Our motivation here is twofold. First, the proposed algorithm for generating fragmented sea ice easily fits into the underlying nonlinear formulation (6) and (7) and thus is suitable for direct numerical simulation. Second, it is primarily intended to describe wave scattering by an array of separate ice floes, modulo a number of simplifying assumptions in addition to the thin-plate related approximations mentioned earlier. These additional assumptions include the following.

(i) As a consequence of the continuity of the physical variables and their derivatives across the ice-water boundaries, the ice floes are not allowed to float freely (no free edges).

(ii) The floe distribution is fixed in space and time, so there is no feedback from waves to floes. In particular, ice breaking under wave action and the subsequent development of cracks and leads
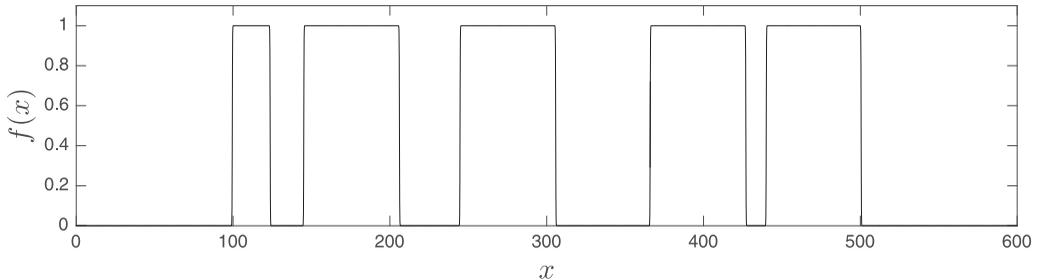
FIG. 1. One realization of the spatial variation $f(x)$ for the coefficient of flexural rigidity. The ice cover spans a distance $L_c = 400$ between $x = 100$ and $x = 500$ and consists of $N_f = 5$ floes whose individual length is specified to be $L_f = 60$ with $L_w = 1$.

are neglected. Accordingly, the ice floes are not allowed to drift and their number is not allowed to vary. This also implies that frictional effects due to, e.g., floe-floe collisions are not considered.

In our two-dimensional procedure for simulating a fragmented ice cover, its total horizontal extent L_c and the total number N_f of constitutive floes are given parameters. We first generate a regular array of N_f identical floes whose individual extent is L_f and which are equispaced over L_c. Then, to make this arrangement look more irregular (and thus more realistic), each floe is shifted by an amount $\theta L_f / 2$ relative to its initial center of gravity, where θ is a random number uniformly distributed between -1 and 1. Occasionally, if two neighboring floes happen to overlap after this shift, the resulting longer floe will further contribute to inhomogeneity of the simulated ice cover. At the edges of each floe, the continuous transition between the two phases is described by a tanh-like profile, typically

$$\frac{1}{2} + \frac{1}{2} \tanh\left[2\pi\left(\frac{x - x_c + L_f/2}{L_w} + \frac{1}{2}\right)\right], \tag{9}$$

from open water (0) to pack ice (1), and similarly for the transition from pack ice to open water. The parameter x_c denotes the shifted center of gravity of the ice floe and L_w represents the width of this transitional region. As stated above, the tanh function in Eq. (9) is set up so that the phase transition is steep but smooth enough to span a few grid sizes around the floe edge at $x = x_c - L_f/2$.

Figure 1 illustrates one realization of the spatial variation $f(x)$ for the coefficient of flexural rigidity over the entire domain $[0, L] = [0, 600]$. In this example, $L_w = 1$ and there are $N_f = 5$ floes of given length $L_f = 60$ that are randomly distributed over $[100, 100 + L_c] = [100, 500]$ (hence $L_c = 400$). The ice floes are represented by the plateaus $f(x) = 1$. Because they are required to lie within $[100, 500]$, those that have been shifted outside this range are cut off (like the first floe in Fig. 1, which has been significantly shifted to the left by the randomization procedure). Again, this effect is not viewed as detrimental because it further contributes to inhomogeneity of the simulated ice cover. The choice $L_w = 1$ was based on several trials and will be used in all the simulations presented here. This value of L_w was deemed to be a good compromise, being not too small near the grid size and not too large so that the individual floes are clearly distinguishable.

The resulting equations are discretized in space by a pseudospectral method based on the fast Fourier transform. The computational domain spans the interval $0 \leqslant x \leqslant L$ with periodic boundary conditions and is divided into N collocation points. Due to its analyticity properties, the DNO is expressed in the form of a truncated Taylor series where a small number of terms (typically $M < 10$) is sufficient to achieve highly accurate results. Time integration is performed in the Fourier space so that the linear terms can be solved exactly by the integrating factor technique. The nonlinear terms are integrated in time using a fourth-order Runge-Kutta scheme with constant step Δt. Further details on this so-called high-order spectral approach can be found in previous work [22,30,42].

Because incident solitary waves remain essentially localized as they travel across the ice field, computations are run until the main pulse reaches the other end of the domain. Expectedly, the

scattering by ice floes was found to produce small-amplitude short waves that radiate backward from the main pulse but these tend to contaminate the advancing solution by reentering the domain from the other end due to the periodic boundary conditions. To overcome this difficulty, we specify a sponge layer by adding a damping pressure term of the form

$$-\frac{\nu(x)G(\eta)\xi}{\sqrt{1+(\partial_x\eta)^2}} \tag{10}$$

to the right-hand side of (7), where $\nu(x)$ is a tunable spatially dependent coefficient that is nonzero only in a small region near each end of the domain and away from the ice sheet. A tanh profile like (9) is again used to represent the localized spatial behavior of $\nu(x)$. We also note that, although randomly distributed floes are specified here in an effort to mimic the MIZ, it is likely that a similar process of wave scattering and attenuation would take place in this nonlinear setting if periodic floe arrangements were instead used.

III. NUMERICAL RESULTS

Based on this nonlinear wave-ice model, we now present direct numerical simulations aimed at examining the attenuation of solitary waves due to scattering by fragmented sea ice. We set $h = 1$ so that it corresponds to the unit length scale and we typically use $L = 600$, $N = 4096$, $\Delta t = 0.002$, and $M = 6$. Previous extensive tests (in the case of gravity waves on open water and flexural-gravity waves along a continuous ice sheet) have demonstrated that the choice $M = 6$ yields highly accurate results at a reasonable cost [23,43,44]. Before discussing our main results for the problem under consideration, we perform a set of simulations to compare and further test our predictions against a different numerical model.

A. Comparison with the boundary integral method

For a continuous ice sheet of infinite extent, the high-order spectral approach has been validated via direct comparison with numerical results by a boundary integral method [22,23]. Similarly here, we assess the performance of our numerical approach in the case of fragmented sea ice and, for illustration, we examine the simple case of a single floe whose size is comparable to the wavelength. The boundary integral method is designed in such a way that it computes localized traveling waves that are stationary in a reference frame moving at constant speed c. Defining $X = x - ct$, the stream function Ψ is introduced to define the complex potential $w(z) = \Phi(X,y) + i\Psi(X,y)$. The physical plane $z = X(w) + iy(w)$ is mapped to $w(z)$ in the inverse plane where the fluid domain identifies with a uniform strip [45]. In terms of these variables, the fluid-ice interface is represented by

$$[X(\Phi),y(\Phi)] = [X(\Phi+i0),y(\Phi+i0)].$$

Application of Cauchy's integral formula along a rectangular strip between $\Psi = 0$ and $\Psi = -2ch$ yields

$$X'(\Phi_0) - \frac{1}{c} = -\frac{1}{\pi}\int_{-\infty}^{\infty}\frac{y'(\Phi)}{\Phi-\Phi_0}d\Phi, \tag{11}$$

where $X'(\Phi)$ and $y'(\Phi)$ denote the values of $\partial_\Phi X$ and $\partial_\Phi y$ evaluated at the interface $\Psi = 0$.

The single (moving) floe is specified by

$$f(X) = \tfrac{1}{2}[\tanh(20+X) + \tanh(20-X)], \tag{12}$$

whose size is $L_f \simeq 40$. Because steadily progressing wave solutions of (1)–(4) are unlikely to exist in this context, we consider ice deflections produced by a localized pressure distribution (e.g., due to a moving load)
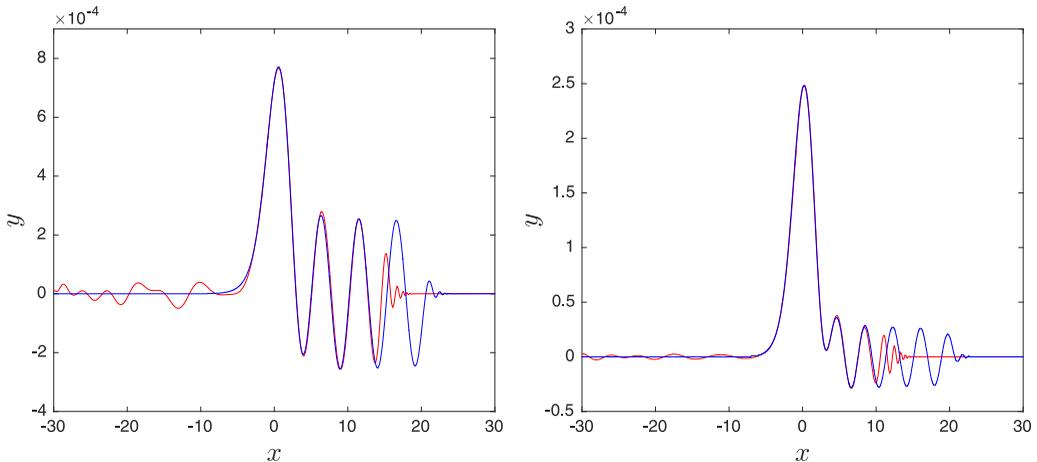
$$P(X) = P_0 e^{-X^2/4}, \tag{13}$$

FIG. 2. Comparison of profiles of η as computed by the boundary integral method (blue line) and the high-order spectral method (red line) for $P_0 = 10^{-3}$ with $c = 1.5$ at $t = 460$ (left) and $c = 2.2$ at $t = 435$ (right). The ice floe lies between $x = -20$ and $x = 20$.

which is added to the left-hand side of (3). The dynamic condition (3) then becomes

$$\frac{1}{2}\left(\frac{1}{X'^2 + y'^2} - c^2\right) + y + f(X)\left(\partial_s^2 \kappa + \frac{1}{2}\kappa^3\right) + P(X) = 0. \tag{14}$$

Equations (11) and (14) are solved for the unknown functions $X(\Phi)$ and $y(\Phi)$ following the numerical method described in detail by Vanden-Broeck and Dias [45] and Guyenne and Părău [23]. The system is discretized by choosing n equally spaced points $\Phi_j = j\Delta\Phi$ ($j = 1, \ldots, n$) and all derivatives are approximated by finite differences. A no-radiation condition is imposed at Φ_1 and the nonlinear system is solved by Newton's method. Typical resolutions $\Delta\Phi = 0.025$ or $\Delta\Phi = 0.05$ are used in the quadrature of (11) and (14) with $n = 3600$ grid points.

On the other hand, in time-dependent simulations of (6) and (7), such forced waves are generated by continually applying (13), starting from zero initial conditions. Similar to (3), Eq. (7) is adjusted to accommodate (12) and (13). To minimize the generation of radiative waves due to a cold start, we also apply a tanh-like ramp function of time to (13), which allows for a smooth transition from 0 to P_0. Despite our effort, however, spurious oscillations were inevitably excited by the applied pressure. The higher the value of P_0, the larger the amplitude of these parasitic waves. For this reason, we choose a small value of P_0 (hence small wave amplitudes) so that we can make a meaningful comparison of the two numerical methods. Moreover, because the periodic boundary conditions may promote amplification of such spurious modes in the time-dependent setting, two moving sponge layers (as defined in Sec. II C) are specified symmetrically at some distance away from the ice floe (12).

The goal here is not to test the proposed physical model of wave-ice interactions, since both numerical approaches consider the same original equations, but rather to test the lower-dimensional formulation (6) and (7), the series expansion of the DNO, and their numerical approximations against an independent computer code in this specific physical situation. Figure 2 presents a direct comparison of wave profiles computed by the boundary integral and high-order spectral methods for $P_0 = 10^{-3}$ with $c = 1.5$ and $c = 2.2$. Solutions from the latter scheme are represented at times much longer than the initial relaxation lapse of (13). Each graph plots the two profiles in such a way that the locations of their highest crests coincide. The ice floe lies in the interval $-20 < x < 20$ and is not depicted to avoid cluttering Fig. 2. Overall, the agreement is found to be quite satisfactory, especially in the neighborhood of the main pulse. Small discrepancies are observed behind the main pulse and near the ice-water transition ahead of it. As discussed above, these differences are attributable to the

solution initialization and resulting unsteadiness in the high-order spectral algorithm. Furthermore, because the hodograph transformation to the (Φ, Ψ) plane implies a varying spatial discretization in the boundary integral method, this may promote generation of dispersive waves near the floe edges where there is a steep phase transition, which thus may also contribute to the observed discrepancies.

B. Wave attenuation

Turning our attention to the nonlinear problem of wave scattering and attenuation through an array of ice floes, we solve (6) and (7) with incident wave conditions given by solitary waves that satisfy the full equations (1)–(4) for surface gravity water waves (i.e., $\sigma = 0$). Of particular interest here is the shallow-water (also called long-wave) regime that is characterized by pure solitary waves with a single localized hump. Such solutions are computed by a boundary integral method based on Cauchy's integral formula and have been extensively tested via time-dependent simulations using our high-order spectral scheme [43]. When unperturbed (e.g., in the absence of ice), they propagate steadily without change of shape and speed.

In the following analysis, we will set $L_c = 400$ with the fragmented ice sheet lying between $x = 100$ and $x = 500$. The main objective is to quantify the attenuation of solitary waves propagating over this distance, as a function of incident wave height A, ice concentration $C \simeq N_f L_f / L_c$, and ice fragmentation $F \simeq N_f$. The quantities $N_f L_f / L_c$ and N_f should be viewed as average values of C and F since their exact values may slightly vary from one realization to another due to floe merging and trimming by the randomization procedure. The attenuation rate will be estimated in an average sense by least-squares fitting continuous curves to discrete numerical data and by considering several realizations of the floe distribution for given values of C and F. However, because of the high computational cost associated with solving a nonlinear nonlocal system of partial differential equations in space and time, only a relatively small ensemble of such realizations will be generated for each set of parameter values.

Numerical data of interest are the spatial L^∞ and L^2 norms of the ice deflection η over the entire computational domain, since their decay in time should be a good indicator of the solitary wave attenuation. The L^∞ norm

$$\|\eta\|_\infty = \sup_{0 \leqslant x \leqslant L} \eta(x,t) \tag{15}$$

is the maximum wave elevation at a given instant, while the L^2 norm

$$\|\eta\|_2 = \left(\frac{1}{L} \int_0^L \eta(x,t)^2 dx \right)^{1/2} \tag{16}$$

is a standard deviation relative to the zero mean value of η (i.e., the quiescent level). Equation (15) provides a natural measure for the decay in wave amplitude due to the solitary wave scattering. On the other hand, the resulting multiple reflections may lead to wave amplification (possibly exceeding the incident amplitude) through constructive interference. Depending on the ice floe arrangement and incident wave condition, such interference may provoke local outbursts in space and time or may have a more global effect causing the wave amplitude to gradually grow over an extended period of time. As for Eq. (16), it is a measure of dispersion (i.e., loss of coherency) of the solitary wave. The smaller this L^2 norm, the closer the solution to a small-amplitude dispersive wave with zero mean value. Because of the squared dependence on η, Eq. (16) may also be interpreted as some wave energy.

We will show numerical results for the range of incident wave heights $A = 0.01, 0.02, 0.05, 0.1,$ 0.2, and 0.3 (relative to $h = 1$). For $A > 0.3$, strong wave focusing due to constructive interference leads to uncontrollable numerical instability and code breakdown. For $A < 0.01$, truncation of the initial wave profile so it can fit into the computational domain (near the left edge of the ice cover) promotes undesirable dispersive effects. This is due to the peculiar fact that the lower the solitary wave, the broader it is. Truncation effects may be minimized in this case by incorporating a very large

portion of the initial solitary wave, but this would require us to specify a prohibitively long domain in total (which is associated with a higher computational cost). A measure of the spatial extent of these incident solitary waves is given by their width W at one-tenth of their height, i.e., $W = 26.36$, 24.02, 18.16, 13.47, 9.96, and 8.49 for $A = 0.01, 0.02, 0.05, 0.1, 0.2$, and 0.3, respectively.

We will consider realizations from four different floe configurations defined by $(N_f, L_f) = (31,4), (31,8), (5,60)$, and $(5,72)$ and corresponding to average ice concentrations $C = 0.31, 0.62$, 0.75, and 0.90, respectively. Among them, two pairs of configurations display well distinct ice fragmentations: one pair $(N_f, L_f) = (31,4)$ and $(31,8)$ is particularly fragmented, composed of many small floes, while the other pair $(N_f, L_f) = (5,60)$ and $(5,72)$ is less fragmented, consisting of much fewer but larger floes. Each pair has two configurations with varying floe sizes, hence varying ice concentrations, but L_f was not varied too much in order to ensure a certain level of ice fragmentation and avoid the risk of excessive floe merging by the randomization procedure. Typically, the larger N_f and L_f (i.e., the higher C), the closer the floe configuration to a continuous ice sheet. Among these four configurations, the case $(N_f, L_f) = (31,4)$ should be closest to open-water conditions since it has the lowest C and highest F, while the case $(N_f, L_f) = (5,72)$ should be most similar to a continuous ice sheet since it has the highest C and lowest F. For this reason, we will pay particular attention to the intermediate cases $(N_f, L_f) = (31,8)$ and $(5,60)$, which serve as a good compromise displaying a nontrivial combination of ice concentration and fragmentation. Note that these two cases exhibit relatively close levels of ice concentration but well distinct levels of ice fragmentation.

First, to show what the attenuation process and various floe configurations look like in the physical space, Figs. 3–6 provide snapshots of η at a few instants during wave propagation across the ice field. One particular realization of each of the floe settings is considered and, as an illustration, we only present results for $A = 0.3$ since wave attenuation is especially pronounced in this regime. This point will be highlighted below in the discussion of decay rates. For graphical purposes, the individual floes are associated with the values of $f(x) \in [1 - \epsilon, 1 + \epsilon]$ (with $\epsilon = 10^{-3}$) to take floating-point arithmetic into account. As presented in Fig. 3, the incident solitary wave is initially located at $x = 80$ near the left edge of the ice cover and travels from left to right. In all cases, its interaction with the random array of ice floes gives rise to an irregular pattern of wave scattering whose characteristics and associated wave decay depend on the levels of ice concentration and fragmentation.

Generally speaking, short floes tend to induce energy loss via small radiation associated with multiple wave reflections (Figs. 3 and 4), while long floes cause the solitary wave to spread and split into moderately large undulations that disperse away in the form of a wave packet along with smaller radiative waves in the far field (Figs. 5 and 6). However, overall, the incident wave retains a core identity since we are able to unambiguously discern a dominant crest and track it throughout the entire propagation. For the sparsest floe configuration $(N_f, L_f) = (31,4)$, Fig. 3 confirms that the initial solitary wave travels essentially unaffected aside from some low level of radiation and slight decrease in amplitude. By contrast, for $(N_f, L_f) = (31,8)$ as illustrated in Fig. 4, the incident wave quickly decays through backward radiation and pulse spreading, but it retains a well-localized shape without splitting into distinct pieces. Comparison of Figs. 3 and 4 indicates that the ice cover should be sufficiently fragmented and dense for wave attenuation to be significant, with a floe size on the order of the wavelength or pulse extent.

As part of the scattering process described above, a noticeable difference between the short-floe configurations $(N_f, L_f) = (31,4)$ and $(31,8)$ and long-floe configurations $(N_f, L_f) = (5,60)$ and $(5,72)$ is a disposition of the latter to generate a moderately large dispersive wave train that propagates forward ahead of the main pulse. This phenomenon is even more apparent in the limiting situation of a single continuous floe spanning the whole ice field (i.e., $N_f = 1$ and $L_f = L_c = 400$), as depicted in Fig. 7, and thus it is likely related to flexural effects. Accordingly, it may be explained in the asymptotic framework of the fifth-order KdV equation for long waves on a continuous ice sheet. This equation admits so-called generalized solitary wave solutions in the sense that they are not truly localized unlike pure solitary waves but consist of a central pulse with oscillatory tails. The occurrence of two tails (one on each side of the pulse) is not possible in the present unsteady regime because otherwise this would imply that there are a wave source and sink at infinity. As discussed
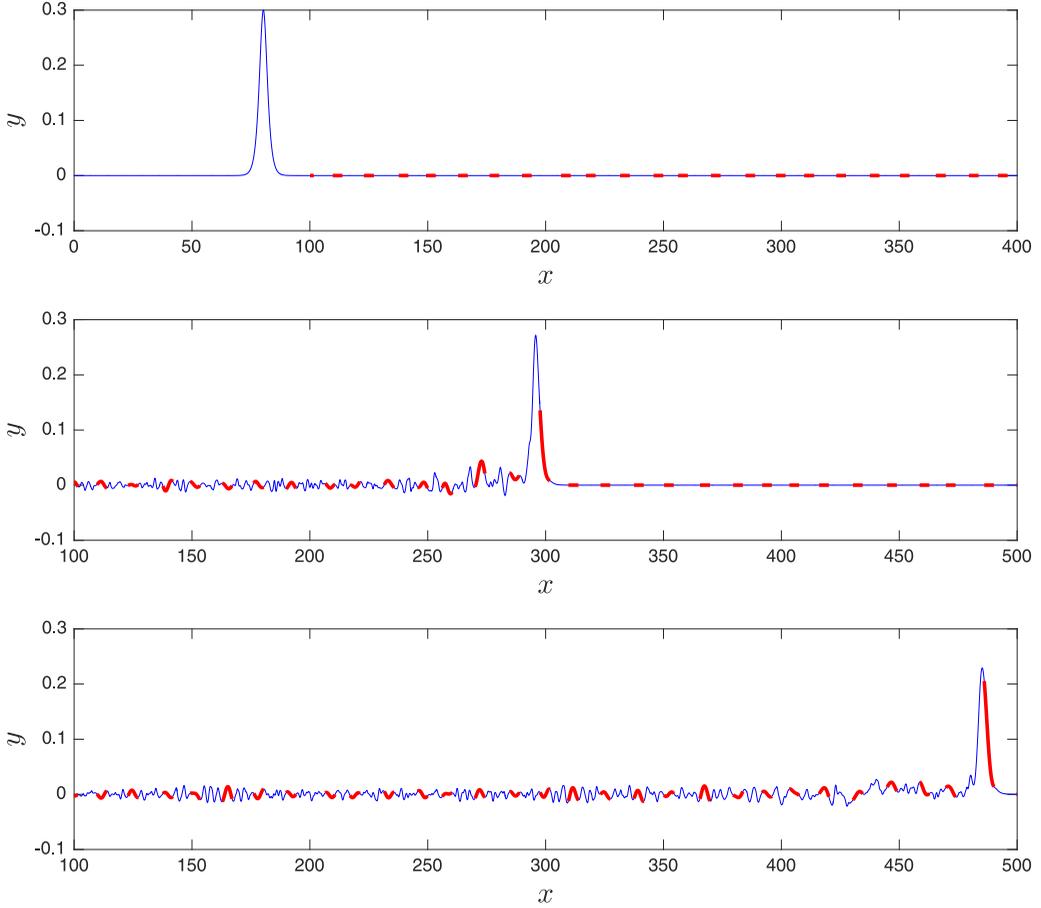
FIG. 3. Snapshots of η at $t = 0$ (top), $t = 190$ (middle), and $t = 360$ (bottom) for $A = 0.3$ and one realization of $(N_f, L_f) = (31,4)$. Open water is represented in blue while ice floes are represented in red.

by Michallet and Dias [46], on which side a dispersive tail appears is determined by the value of its group velocity relative to that of its phase velocity. If the group velocity is less than the phase velocity, then ripples develop behind the solitary pulse; otherwise they appear ahead of it. In the present hydroelastic problem, the group velocity is less than the phase velocity if $k < k_{\min}$ and larger otherwise. The wave number associated with a dispersive tail is naturally given by the resonance condition

$$c_d(k) \equiv 1 - \tfrac{1}{6}k^2 + \tfrac{199}{360}k^4 = c_s, \tag{17}$$

where c_d denotes the fifth-order KdV approximation of (8) in dimensionless units and c_s is the speed of the initial solitary wave. Indeed, Fig. 7 shows that ripples are emitted soon after the incident wave impinges on the ice sheet. As time progresses, the resulting wave train spreads out while the main pulse decays and slows down.

Setting $g = 1$, $\sigma/\rho = 1$, and $h = 1$ in Eq. (8), the value $k_{\min} = 0.399$ is found numerically where this dispersion relation achieves its minimum $c_{\min}$ [i.e., where the first derivative $c'(k) = 0$]. Because Eq. (17) is a quadratic algebraic equation for k^2, it can be solved exactly. The relevant wave number k is determined by selecting the positive root of (17) and then, without loss of generality, by taking the positive square root of this value. For $A = 0.3$, we get $c_s = 1.137$ (from the boundary integral method that computes solitary water waves) and thus $k = 0.820$. This result confirms that ripples should
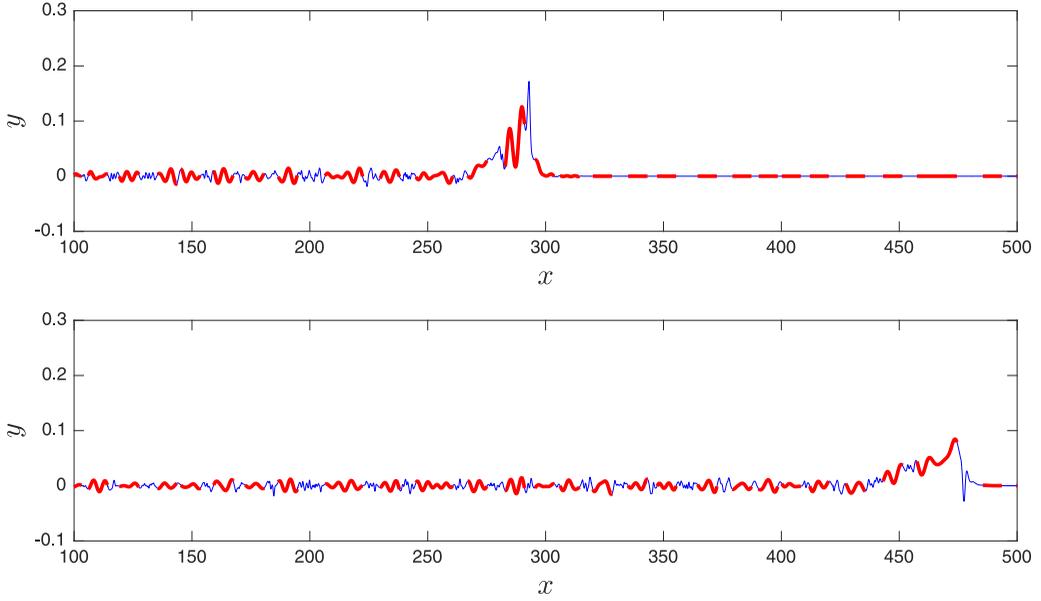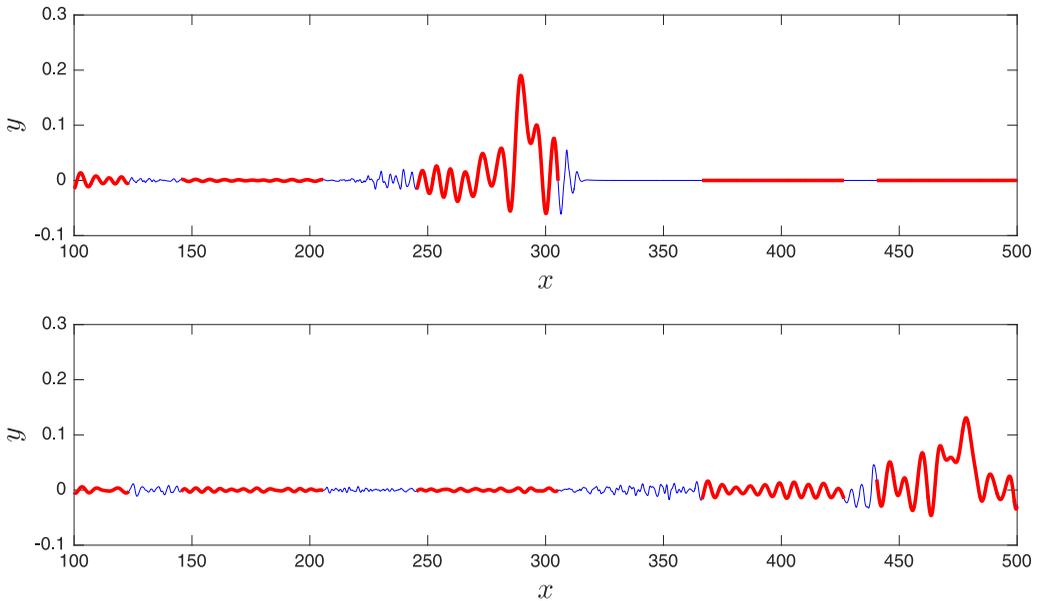
FIG. 4. Snapshots of η at $t = 190$ (top) and $t = 360$ (bottom) for $A = 0.3$ and one realization of $(N_f, L_f) = (31,8)$. Open water is represented in blue while ice floes are represented in red.

indeed appear ahead of the main pulse because $k > k_{\min}$, and we have graphically checked that the dispersive wavelength is about $\lambda = 2\pi/k = 7.666$ in Fig. 7. A similar calculation was performed by Guyenne and Părău [23] to analyze flexural-gravity waves propagating along a continuous ice sheet of infinite extent on shallow water. It is clear from (17) why the higher-order $O(k^4)$ contribution should be added to the usual KdV terms $1 - k^2/6$ because otherwise $c_d(k) < c_0 = \sqrt{gh} = 1$ (in

FIG. 5. Snapshots of η at $t = 190$ (top) and $t = 360$ (bottom) for $A = 0.3$ and one realization of $(N_f, L_f) = (5,60)$. Open water is represented in blue while ice floes are represented in red.
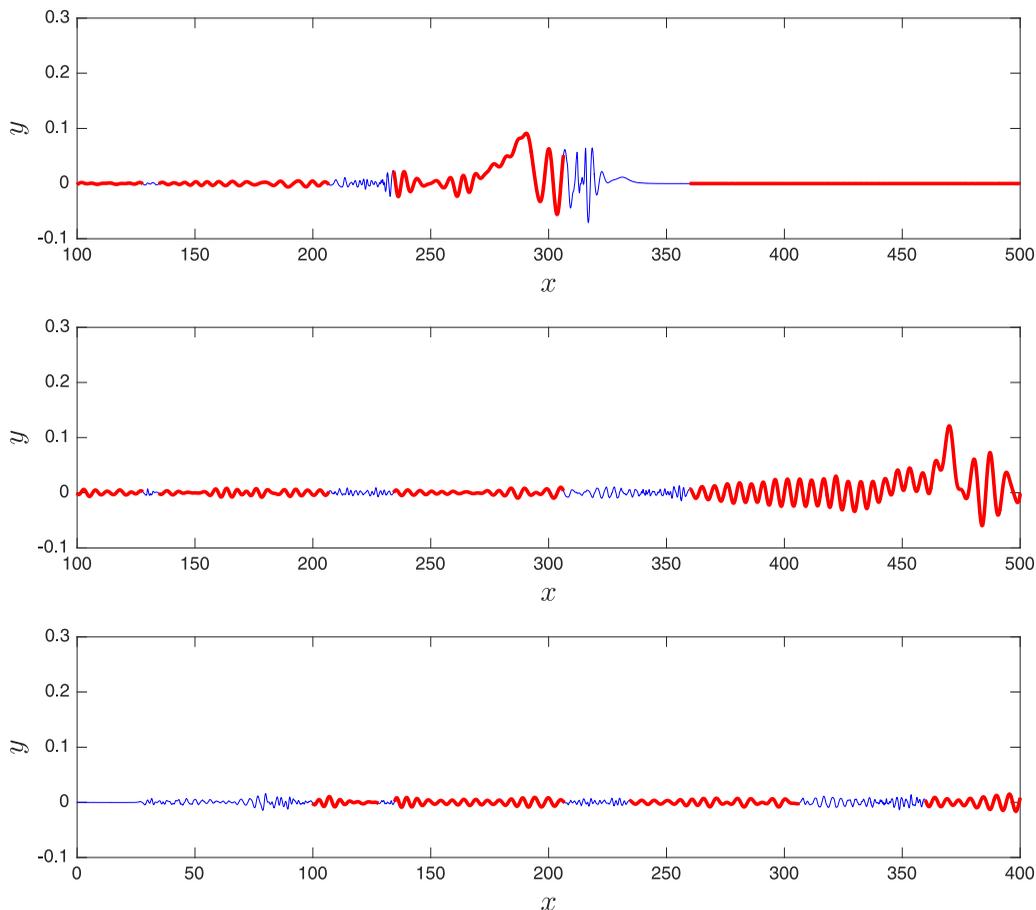
FIG. 6. Snapshots of η at $t = 190$ (top), $t = 360$ (middle), and $t = 370$ (bottom) for $A = 0.3$ and one realization of $(N_f, L_f) = (5, 72)$. Open water is represented in blue while ice floes are represented in red.

dimensionless units), which would conflict with $c_s > c_0$. This would imply no possible resonance for any $k \neq 0$ and hence no dispersive tail.

The snapshot of η at the late instant $t = 370$ in Fig. 6 illustrates the effectiveness of the pressure term (10) at absorbing small waves that radiate backward from the incoming pulse. The corresponding sponge layer is recognizable by the relative calmness near the left end of the computational domain (for $0 \leqslant x \lesssim 30$). Another sponge layer (not shown here) is specified near the opposite end to absorb possible undesirable forward-moving radiation. Figure 8, displaying close-ups of η around floe edges, is intended to demonstrate the continuity and smoothness of η there, as claimed earlier. One close-up shows η under a wave disturbance of small amplitude between two ice floes far behind the main pulse in the configuration $(N_f, L_f) = (31, 8)$, while the other close-up presents a steeper profile of η around a floe edge being passed by the incoming wave for $(N_f, L_f) = (5, 60)$. On both graphs, no jumps or onset of numerical instabilities are detectable at the ice-water transitions.

To further quantify the observed attenuation, Figs. 9 and 10 depict the L^∞ norm (15) and L^2 norm (16), respectively, as functions of time for one realization of the floe configuration $(N_f, L_f) = (31, 8)$. Data for $A = 0.01$–0.3 are shown from the time the main pulse of the solitary wave enters to the time it exits the ice field. As a reference, data for the single long floe $(N_f, L_f) = (1, 400)$ are also plotted on the graphs. These numerical results are normalized relative to the incident values at $t = 0$. In the literature, a simple exponential decay with distance traveled through sea ice has typically been
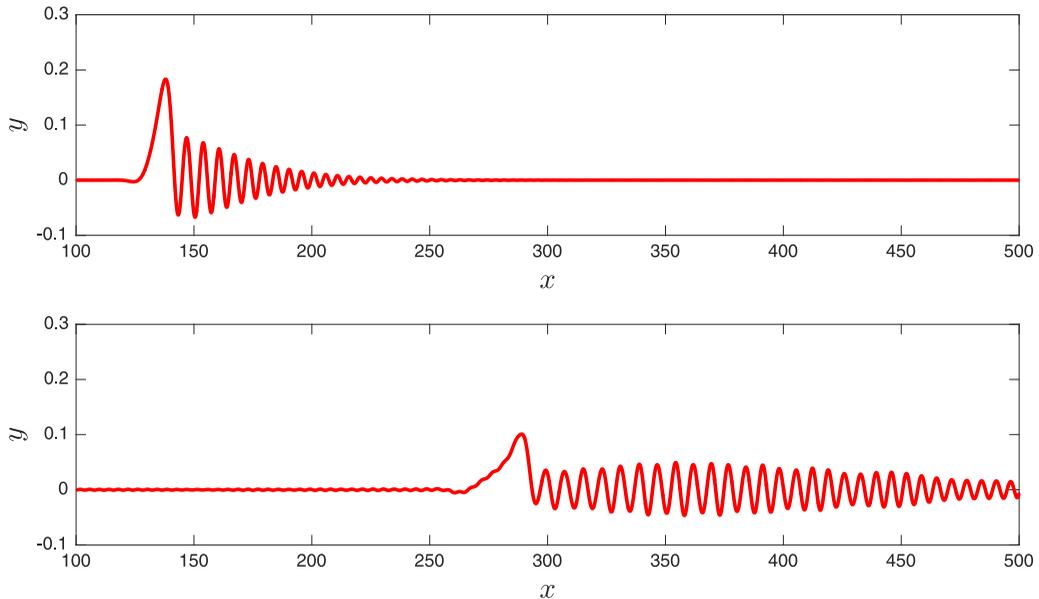
FIG. 7. Snapshots of η at $t = 50$ (top) and $t = 190$ (bottom) for $A = 0.3$ and a single long floe $(N_f, L_f) = (1,400)$.

reported for small-amplitude waves based on scattering theory [7,9,12], while recent observations of Kohout *et al.* [15] provided evidence of a slower near linear decay for large-amplitude waves. To take these two possible trends into account, both linear and exponential fits by least squares are also presented here for each data set. Although we look at wave characteristics as functions of time, there is a direct correspondence to the behavior as a function of distance traveled into the ice field (even in this nonlinear regime) owing to the localized and progressive nature of solitary waves. Moreover, in view of potential implications for operational wave forecasting models, it is of particular interest to examine the temporal evolution directly.

A number of general observations can be made from Figs. 9 and 10. First, the data for (15) are more spread out than those for (16), which is consistent with the fact that the L^∞ norm gives a single instantaneous value, while the L^2 norm is a spatially averaged quantity. The data for a multiple-floe configuration are also more spread out than those for a single-floe configuration, which is a sign of stronger wave scattering in the former case due to multiple wave reflections caused by the ice floes. However, this does not necessarily imply stronger wave attenuation because constructive wave
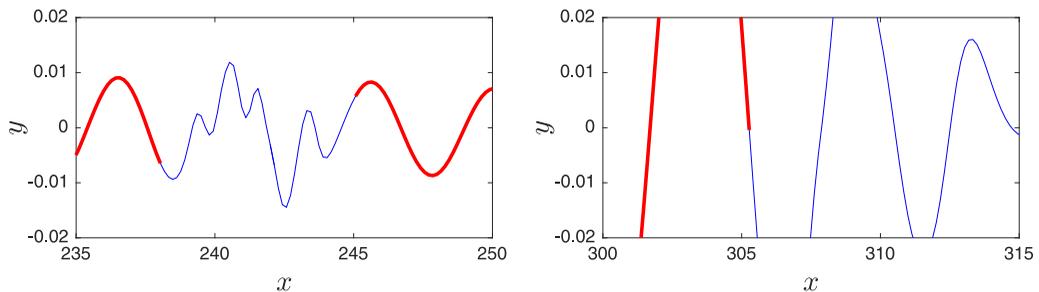

FIG. 8. Close-up of η at $t = 360$ from Fig. 4 (left) and at $t = 190$ from Fig. 5 (right) for $A = 0.3$. The corresponding floe configurations are $(N_f, L_f) = (31,8)$ and $(5,60)$, respectively. Open water is represented in blue while ice floes are represented in red.
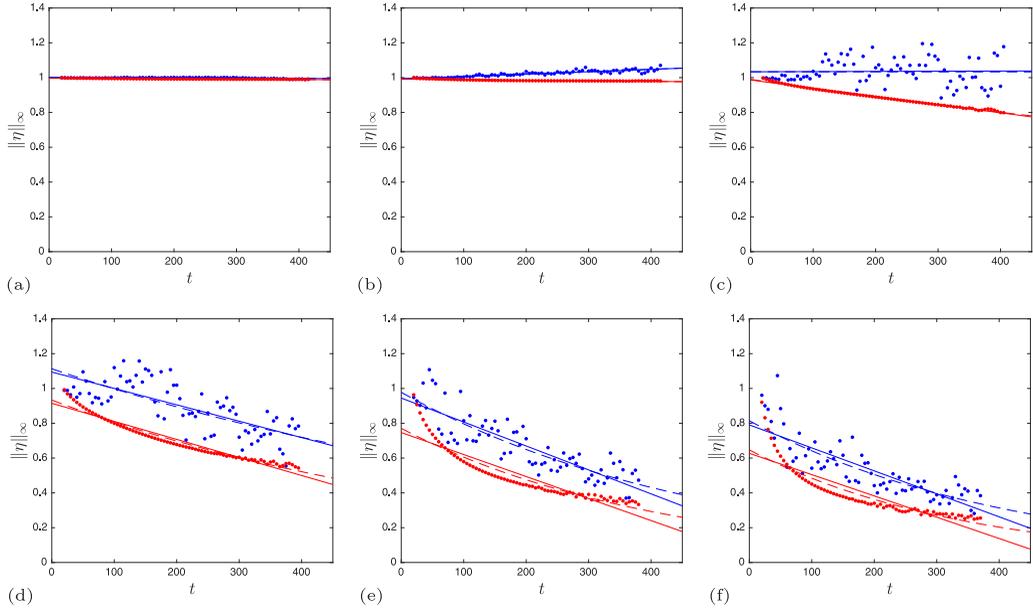
FIG. 9. The L^∞ norm of η as a function of time for (a) $A = 0.01$, (b) $A = 0.02$, (c) $A = 0.05$, (d) $A = 0.1$, (e) $A = 0.2$, and (f) $A = 0.3$. Numerical data for one realization of $(N_f, L_f) = (31, 8)$ are plotted as blue dots while those for a single long floe $(N_f, L_f) = (1, 400)$ are plotted as red dots. For each data set, the linear fit is plotted as a solid line while the exponential fit is plotted as a dashed line.
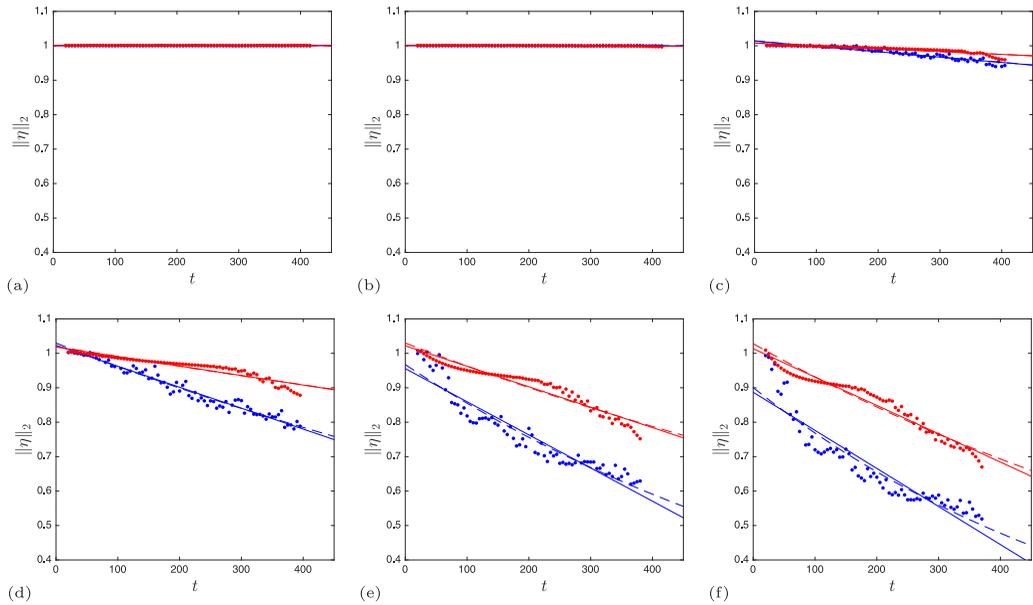

FIG. 10. The L^2 norm of η as a function of time for (a) $A = 0.01$, (b) $A = 0.02$, (c) $A = 0.05$, (d) $A = 0.1$, (e) $A = 0.2$, and (f) $A = 0.3$. Numerical data for one realization of $(N_f, L_f) = (31, 8)$ are plotted as blue dots while those for a single long floe $(N_f, L_f) = (1, 400)$ are plotted as red dots. For each data set, the linear fit is plotted as a solid line while the exponential fit is plotted as a dashed line.

interference may occur. For either the single- or multiple-floe configuration, examination of either the L^∞ or L^2 norm indicates that wave attenuation is more severe as A is increased, in the sense that L^∞ and L^2 values are overall lower and their decay over time is steeper. Scattering effects are barely discernible for low amplitudes ($A < 0.05$), while the attenuation is quite pronounced for high amplitudes ($A > 0.05$). This is compatible with linear scattering theory and field observations that show a decrease in attenuation as the wave period (or equivalently the wavelength) increases [7,12]. For the solitary wave forcing being considered, the lower the amplitude, the less localized the pulse, so the solution may be viewed as a wave with large wavelength, which therefore experiences little scattering. Differences between the single- and multiple-floe configurations are also more significant as A is increased.

For small wave amplitudes, we see that the numerical data are well approximated by a linear function of time $\|\eta\| = \alpha t + \beta$ in all cases. The exponential fit

$$\|\eta\| = \beta e^{\alpha t} \tag{18}$$

is found to be so slowly varying that it is indistinguishable from the linear fit. As A is increased, the data exhibit a more nonlinear decay in time, with a more convex profile and accordingly with a more distinctive exponential fit. We note, however, that, even in this parameter regime, the exponential function (18) does not seem to provide a much better approximation to the numerical results than the linear fit does. The reason is because the data seem to converge to a nonzero (positive) limit rather than to zero as time goes on. For $A = 0.3$ (highest incident amplitude considered), this more convex decay is apparent in both single- and multiple-floe graphs of the L^∞ norm as well as in the multiple-floe graph of the L^2 norm, while a straight line still fits well the single-floe data for the L^2 norm.

Overall, solitary wave scattering and attenuation by an array of ice floes are clearly indicated on these graphs of (15) and (16). In particular, wave attenuation is well represented by the systematic decay of the L^2 norm over time for the entire range of wave amplitudes being considered and also, to a lesser extent, by the L^∞ norm decay. An exception is the slow growth of the L^∞ norm, which is observed for low amplitudes ($A < 0.1$) in the multiple-floe configuration. As hinted at earlier, a possible explanation for this phenomenon is constructive interference between the incoming solitary wave and successive wave reflections induced by the ice floes, which is promoted by the broader support of solitary waves at lower amplitudes, thus allowing in-phase wave superposition to more likely occur. Although the local maximum elevation (15) may grow over time by such a process, the wave would still distort, scatter, and radiate energy as it travels across the ice field, thus contributing to the decay of (16) as shown in Fig. 10. We further note that the case $(N_f, L_f) = (31,8)$ corresponding to well-fragmented sea ice is particularly effective at scattering and attenuating incoming waves. It does a significantly better job than the single-floe configuration in this regard, leading to lower L^2 values that also decline faster over time, especially at large wave amplitudes.

Similar statements can be made for $(N_f, L_f) = (5,60)$ as described in Figs. 11 and 12, including the growing trend of (15) at small wave amplitudes. In fact, this phenomenon is also observed in the other two cases $(N_f, L_f) = (31,4)$ and $(5,72)$. Although we may not directly associate this result with the field observations of Wadhams *et al.* [12], it is worth pointing out that these authors also reported wave growth rather than attenuation at very long periods from some of their measurements (in Greenland Sea 1978), but they suggested forcing by wind action and wave reflection from the coast as a possible explanation. Considering the multiple-floe results in Fig. 12, a notable difference compared to the previous situation $(N_f, L_f) = (31,8)$ is that the exponential fit does not become more distinctive as A is increased. The corresponding L^2 decay is slower than that for the single-floe configuration, but the two data sets remain relatively close together on the graphs. This indicates that pulse spreading and splitting due to the ice cover itself play a prominent role in wave attenuation for $(N_f, L_f) = (5,60)$, which is consistent with the fact that this case corresponds to less-fragmented sea ice than specified by $(N_f, L_f) = (31,8)$ and thus is likely less effective at scattering incoming waves. Further discussion will be given below when examining the decay rate as a function of ice concentration. We also see significant oscillations in the multiple-floe data of Figs. 11 and 12, which

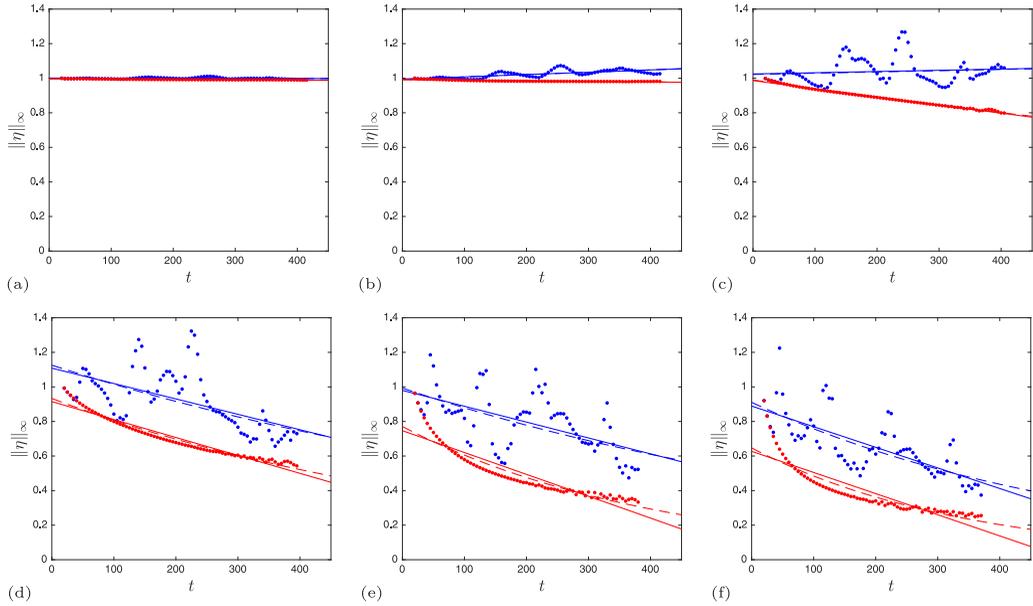FIG. 11. The L^∞ norm of η as a function of time for (a) $A = 0.01$, (b) $A = 0.02$, (c) $A = 0.05$, (d) $A = 0.1$, (e) $A = 0.2$, and (f) $A = 0.3$. Numerical data for one realization of $(N_f, L_f) = (5, 60)$ are plotted as blue dots while those for a single long floe $(N_f, L_f) = (1, 400)$ are plotted as red dots. For each data set, the linear fit is plotted as a solid line while the exponential fit is plotted as a dashed line.
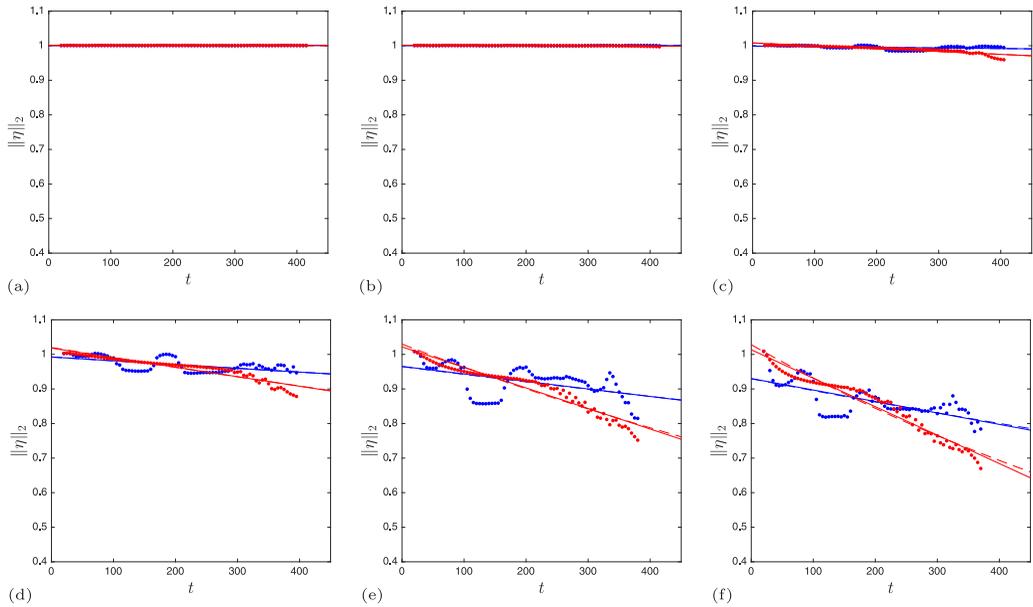

FIG. 12. The L^2 norm of η as a function of time for (a) $A = 0.01$, (b) $A = 0.02$, (c) $A = 0.05$, (d) $A = 0.1$, (e) $A = 0.2$, and (f) $A = 0.3$. Numerical data for one realization of $(N_f, L_f) = (5, 60)$ are plotted as blue dots while those for a single long floe $(N_f, L_f) = (1, 400)$ are plotted as red dots. For each data set, the linear fit is plotted as a solid line while the exponential fit is plotted as a dashed line.
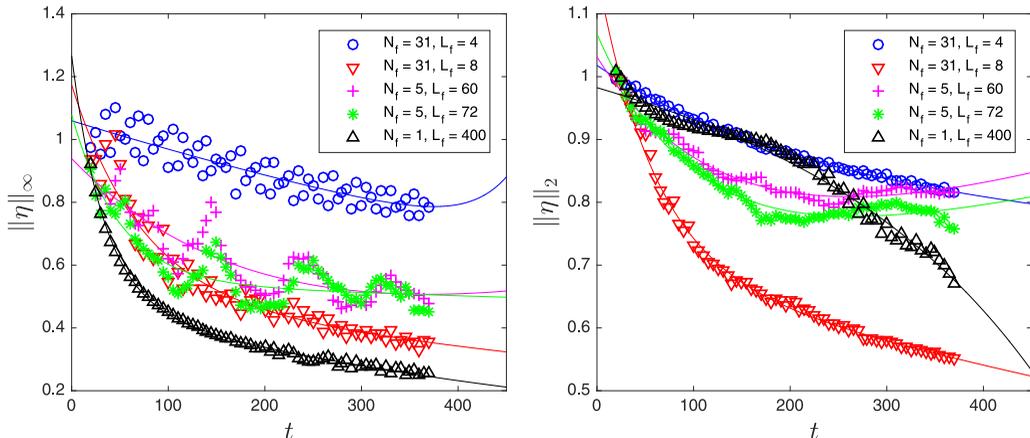
FIG. 13. The L^∞ norm (left) and L^2 norm (right) of η as functions of time for $A = 0.3$. Numerical data averaged over eleven realizations of each of the four floe configurations are plotted as various symbols, while their two-term exponential fits are plotted as a solid line. As a reference, data for the single long floe are also plotted.

may be attributed to the layout of $(N_f, L_f) = (5, 60)$ having extended areas of ice and water as illustrated in Fig. 5. This promotes disturbances as the wave moves from one area to another and thus leads to more fluctuations in both norms of η.

Recognizing that wave attenuation is especially apparent at high amplitudes, Fig. 13 collects L^∞ and L^2 data for $A = 0.3$, which are averaged over eleven realizations of each of the four floe configurations. This allows for a direct comparison among these various configurations using smoother data sets. Results for the single long floe are also plotted as a reference. Modulo the wider spreading of the L^∞ data, these are found to be quite comparable to the L^2 results regarding their variation in time and their dependence on floe parameters. More specifically, the choice $(N_f, L_f) = (31, 8)$ turns out to be the most attenuating one among the four floe configurations. It displays a significantly lower and steeper L^2 decay than the other three cases, including $(N_f, L_f) = (5, 72)$, which is most similar to a continuous ice sheet. This is consistent with a previous statement that $(N_f, L_f) = (31, 8)$ even outperforms the single-floe configuration. As expected, the choice $(N_f, L_f) = (31, 4)$ is the least attenuating one since it is closest to open-water conditions, and the corresponding L^2 decay is such that it could be reasonably well approximated by a linear function of time. However, overall, these smoother data confirm the more convex decreasing trend, especially in floe settings favoring wave attenuation.

Recall that a simple one-term exponential fit such as (18) was used with only moderate success in our previous figures because the data do not seem to fall down to zero over time, at least not as fast as predicted by (18). Instead, we find that they are better approximated by a two-term exponential function of the form

$$\|\eta\| = \beta e^{\alpha t} + \delta e^{\gamma t}, \tag{19}$$

where α and γ are of opposite signs, as presented in Fig. 13 for all cases. This double exponential behavior may be attributed to the cumulative action of multiple wave reflections caused by the floes, expressing the competition between constructive and destructive interference during wave propagation across the ice field. More specific to the incident wave conditions that we are using in this study, another possible explanation has to do with the well-known stability of solitary waves under perturbations, including collisions [43,47]. When traveling through sea ice, solitary waves scatter and distort, but they retain a certain coherence and localized shape due to their strong stability properties as revealed in Figs. 3–6, which may explain why the L^∞ or L^2 norm of η does
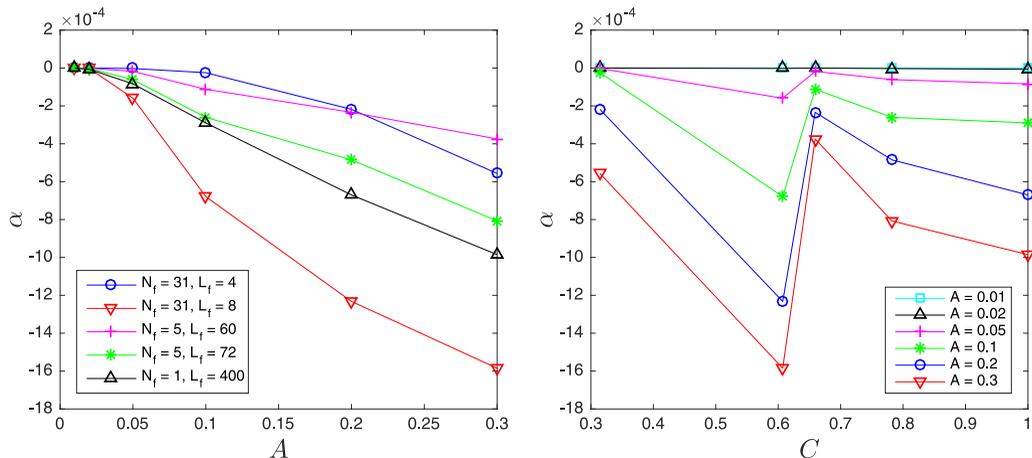
FIG. 14. Exponential rate of attenuation for the L^2 norm of η as a function of incident wave height (left) and ice concentration (right). Numerical data for one realization of each of the four floe configurations are plotted. As a reference, data for the single long floe are also plotted.

not seem to converge to zero as $t \to +\infty$. Aside from this peculiarity, the exponential dependence of (19) for the attenuation of steep solitary waves may be interpreted as supporting evidence for an underlying scattering process similar to linear predictions. A scattering model is usually suitable for short-period waves in sea ice [7,12] and this is probably also true for highly localized pulses. Note that the slight change in behavior (from decreasing to increasing) as suggested by the fit in Fig. 13 for $(N_f, L_f) = (5,60)$ and $(5,72)$ is likely an artifact and may imply the need for considering a larger time interval. This issue is beyond the scope of the present paper.

To further explore the dependence of results on incident wave conditions and floe parameters, we extract a decay rate from L^2 data for one realization of each of the four floe configurations. Due to the higher computational cost that would be involved, we did not run simulations over several floe realizations for the entire range of wave amplitudes. The L^2 norm (16) is preferred for this calculation because it turns out to be a suitable indicator of wave attenuation as suggested in previous figures. The decay rate α is obtained by fitting a simple exponential function of the form (18) to the numerical data. This was found to be sufficient for our purposes since we only need to get some measure of wave attenuation to examine the parametric dependence, rather than using the best possible approximation, which would require a more complex analysis.

Figure 14, showing α as a function of A and C for all four floe configurations, draws a number of comments in support of those made earlier. Note that actual (not average) values of C are indicated here for the floe realizations under consideration. First, the tendency for wave scattering and attenuation (i.e., $\alpha < 0$) is confirmed in all cases. The larger the incident wave amplitude, the higher the decay rate (i.e., $|\alpha|$ increases with A), and scattering effects are negligible for $A = 0.01$ and $A = 0.02$. This is a consequence of the pulse being more localized as A is increased, which approximates shorter waves experiencing more scattering. Overall, the attenuation-rate curves in Fig. 14 exhibit the same order $(N_f, L_f) = (31,4)$, $(5,60)$, $(5,72)$, and $(31,8)$ from the least to the most attenuating floe configuration as that given in Fig. 13 by the attenuation-level curves, with the exception that $(N_f, L_f) = (31,4)$ tends to promote a faster L^2 decay than $(N_f, L_f) = (5,60)$ at larger wave amplitudes.

Another important point highlighted by Fig. 14 is the fact that $(N_f, L_f) = (31,8)$ is significantly more favorable to wave attenuation than $(N_f, L_f) = (5,60)$, although they feature similar levels of ice concentration. Given that the floe configuration $(N_f, L_f) = (31,8)$ is much more fragmented than $(N_f, L_f) = (5,60)$ while being even slightly less concentrated in ice, i.e., $C = 0.61$ and $C = 0.66$, respectively, this clearly indicates that wave scattering is promoted by a high level

of ice fragmentation. However, a certain level of ice concentration is also necessary (i.e., the multiple floes should be long enough) for scattering to be effective; otherwise the incoming solitary wave would experience little pulse spreading and thus would not be significantly affected by these inhomogeneities. This was noticed earlier when comparing Figs. 3 and 4 and is demonstrated again in Fig. 14 for $(N_f, L_f) = (31,4)$ and $(31,8)$, which admit similar values of F but well distinct values of C and α.

In this nonlinear problem, the subtle dependence of wave attenuation on ice concentration and fragmentation reflects the close interplay between two different phenomena involved in the scattering process: (i) wave reflections from the multiple floes and (ii) pulse spreading and splitting due to the presence of ice. For an arbitrary fragmented ice cover, wave attenuation likely results from a complicated superposition of these two effects. The extent to which one of them dominates the attenuation process can be assessed by comparing the single- and multiple-floe configurations in Figs. 13 and 14. Because the L^2 decay for $(N_f, L_f) = (31,8)$ is significantly stronger than that for any other floe configuration including the single-floe one, this pinpoints phenomenon (i) as the main mechanism responsible for wave attenuation in a highly fragmented ice cover. On the other hand, the closer proximity between L^2 data for $(N_f, L_f) = (5,72)$ and $(1,400)$ suggests that phenomenon (ii) plays a more prominent role in the case of more compact sea ice. Examination of the L^∞ data in Fig. 13 reveals that wave amplitude is most severely reduced in the single-floe configuration, even outperforming $(N_f, L_f) = (31,8)$ in this regard. This result further supports the association (to varying extent) of phenomenon (i) with wave attenuation in fragmented sea ice. Indeed, the solitary wave amplitude is found to quickly decrease over time via mechanism (ii) for a continuous uniform ice sheet (see Fig. 7) while, in multiple-floe configurations, mechanism (i) (especially wave reflections from ice floes in the close vicinity of the main pulse) promotes wave focusing through constructive interference and thus leads to a slower L^∞ decay (see, e.g., Fig. 4).

IV. CONCLUSION

We have proposed a numerical model for direct phase-resolved simulation of nonlinear ocean waves interacting with fragmented sea ice. This high-order spectral model solves the full time-dependent equations for nonlinear potential flow, combined with a nonlinear bending force that characterizes the ice cover according to the special Cosserat theory of hyperelastic shells. We have explored the possibility of using an *ad hoc* extension of the original plate formulation so that spatial distributions of ice floes can be directly incorporated into the numerical algorithm. Effort was devoted to specifying irregular samples of such distributions.

Restricting our attention to the two-dimensional finite-depth problem, we have examined the attenuation of solitary waves due to scattering through an array of ice floes. The numerical model was run for various floe configurations and two different measures (L^∞ and L^2 norms of η) were used to quantify wave attenuation and scattering over time as a function of incident wave height, ice concentration, and ice fragmentation. We have obtained a number of numerical results that, despite having peculiarities related to solitary waves, are overall consistent with previous observations from the literature.

(a) The larger the incident wave amplitude or steepness, the stronger the attenuation, which is a consequence of the more localized profile of the pulse.

(b) For small wave amplitudes (corresponding to broad solitary waves in this study), the decay is so slow that it is well approximated by a linear function of time. Unlike the L^2 norm, the maximum wave elevation (i.e., the L^∞ norm of η) tends to grow over time due to constructive interference with multiple wave reflections.

(c) For large wave amplitudes (corresponding to steep solitary waves), the fast decay is best approximated by a double exponential function of time, reflecting the fact that the data seem to converge to a nonzero positive limit. This behavior may be attributed to the strong stability properties of solitary waves.

(d) The sparser the ice cover, the weaker the wave attenuation. For the least attenuating floe configuration that we considered, the slow wave decay is well approximated by a linear function of time even at large amplitudes. As for the most attenuating floe configuration, it represents a good compromise between ice concentration and fragmentation, displaying a floe size on the order of the pulse extent.

The present model should be viewed as a first step to provide a platform for direct phase-resolved simulation of nonlinear ocean waves in the MIZ. Among the possible refinements, we envision to experiment with more realistic incident wave conditions and to include dissipative mechanisms in the sea-ice model. It would be of interest to examine the contribution of such mechanisms to wave attenuation from a deterministic and nonlinear point of view. We would like to extend the present work to the two-dimensional deep-water case. We also would like to investigate the three-dimensional problem with fragmented sea ice and compare with recent field measurements [48,49]. The proposed approach for simulating wave-ice interactions is readily extensible to three dimensions [44]. Preliminary three-dimensional computations were performed by Părău and Vanden-Broeck [50] for nonlinear potential flow coupled with a continuous ice sheet according to linear Euler-Bernoulli theory.

---

[1] J. Stroeve, M. M. Holland, W. Meier, T. Scambos, and M. Serreze, Arctic sea ice decline: Faster than forecast, Geophys. Res. Lett. **34**, L09501 (2007).

[2] J. C. Comiso, C. L. Parkinson, R. Gersten, and L. Stock, Accelerated decline in the Arctic sea ice cover, Geophys. Res. Lett. **35**, L01703 (2008).

[3] I. R. Young, S. Zieger, and A. V. Babanin, Global trends in wind speed and wave height, Science **332**, 451 (2011).

[4] R. Wang and H. H. Shen, Gravity waves propagating into an ice-covered ocean: A viscoelastic model, J. Geophys. Res. **115**, C06024 (2010).

[5] J. E. M. Mosig, F. Montiel, and V. A. Squire, Comparison of viscoelastic-type models for ocean wave attenuation in ice-covered seas, J. Geophys. Res. **120**, 6072 (2015).

[6] M. H. Meylan and D. Masson, A linear Boltzmann equation to model wave scattering in the marginal ice zone, Ocean Model. **11**, 417 (2006).

[7] A. L. Kohout and M. H. Meylan, An elastic plate model for wave attenuation and ice floe breaking in the marginal ice zone, J. Geophys. Res. **113**, C09016 (2008).

[8] L. G. Bennetts and V. A. Squire, Wave scattering by multiple rows of circular ice floes, J. Fluid Mech. **639**, 213 (2009).

[9] L. G. Bennetts and V. A. Squire, On the calculation of an attenuation coefficient for transects of ice-covered ocean, Proc. R. Soc. A **468**, 136 (2012).

[10] F. Montiel, V. A. Squire, and L. G. Bennetts, Attenuation and directional spreading of ocean wave spectra in the marginal ice zone, J. Fluid Mech. **790**, 492 (2016).

[11] V. A. Squire and F. Montiel, Evolution of directional wave spectra in the marginal ice zone: A new model tested with legacy data, J. Phys. Oceanogr. **46**, 3121 (2016).

[12] P. Wadhams, V. A. Squire, D. J. Goodman, A. M. Cowan, and S. C. Moore, The attenuation rates of ocean waves in the marginal ice zone, J. Geophys. Res. **93**, 6799 (1988).

[13] V. A. Squire, Past, present and impendent hydroelastic challenges in the polar and subpolar seas, Philos. Trans. R. Soc. A **369**, 2813 (2011).

[14] J. Thomson and W. E. Rogers, Swell and sea in the emerging Arctic Ocean, Geophys. Res. Lett. **41**, 3136 (2014).

[15] A. L. Kohout, M. J. M. Williams, S. M. Dean, and M. H. Meylan, Storm-induced sea-ice breakup and the implications for ice extent, Nature (London) **509**, 604 (2014).

[16] J. R. Marko, Observations and analyses of an intense waves-in-ice event in the Sea of Okhotsk, J. Geophys. Res. **108**, 3296 (2003).

[17] M. Haragus-Courcelle and A. Ilichev, Three-dimensional solitary waves in the presence of additional surface effects, Eur. J. Mech. B **17**, 739 (1998).

[18] E. Părău and F. Dias, Nonlinear effects in the response of a floating ice plate to a moving load, J. Fluid Mech. **460**, 281 (2002).

[19] F. Bonnefoy, M. H. Meylan, and P. Ferrant, Nonlinear higher-order spectral solution for a two-dimensional moving load on ice, J. Fluid Mech. **621**, 215 (2009).

[20] P. A. Milewski, J.-M. Vanden-Broeck, and Z. Wang, Hydroelastic solitary waves in deep water, J. Fluid Mech. **679**, 628 (2011).

[21] P. I. Plotnikov and J. F. Toland, Modelling nonlinear hydroelastic waves, Philos. Trans. R. Soc. A **369**, 2942 (2011).

[22] P. Guyenne and E. I. Părău, Computations of fully nonlinear hydroelastic solitary waves on deep water, J. Fluid Mech. **713**, 307 (2012).

[23] P. Guyenne and E. I. Părău, Finite-depth effects on solitary waves in a floating ice sheet, J. Fluids Struct. **49**, 242 (2014).

[24] P. Guyenne and E. I. Părău, Forced and unforced flexural-gravity solitary waves, Proc. IUTAM **11**, 44 (2014).

[25] P. A. Milewski and Z. Wang, Three dimensional flexural-gravity waves, Stud. Appl. Math. **131**, 135 (2013).

[26] M. A. Hopkins and H. H. Shen, Simulation of pancake-ice dynamics in a wave field, Ann. Glaciol. **33**, 355 (2001).

[27] G. M. Hegarty and V. A. Squire, A boundary-integral method for the interaction of large-amplitude ocean waves with a compliant floating raft such as a sea-ice floe, J. Eng. Math. **62**, 355 (2008).

[28] M. J. Doble and J.-R. Bidlot, Wavebuoy measurements at the Antarctic sea ice edge compared with an enhanced ECMWF WAM: Progress towards global waves-in-ice modeling, Ocean Model. **70**, 166 (2013).

[29] J. Li, A. L. Kohout, and H. H. Shen, Comparison of wave propagation through ice covers in calm and storm conditions, Geophys. Res. Lett. **42**, 5935 (2015).

[30] W. Craig and C. Sulem, Numerical simulation of gravity waves, J. Comput. Phys. **108**, 73 (1993).

[31] K. M. Brunt, E. A. Okal, and D. R. MacAyeal, Antarctic ice-shelf calving triggered by the Honshu (Japan) earthquake and tsunami, March 11, J. Glaciol. **57**, 785 (2011).

[32] J. Leblanc, D. Turmel, J. Therrien, and J. Locat, in *Submarine Mass Movements and their Consequences*, edited by G. Lamarche *et al.*, Advances in Natural and Technological Hazards Research (Springer, Berlin, 2016), Chap. 61, pp. 607–614.

[33] D. Givoli, Non-reflecting boundary conditions, J. Comput. Phys. **94**, 1 (1991).

[34] R. M. S. M. Schulkes, R. J. Hosking, and A. D. Sneyd, Waves due to a steadily moving source on a floating ice plate. Part 2, J. Fluid Mech. **180**, 297 (1987).

[35] P. Guyenne, D. Lannes, and J.-C. Saut, Well-posedness of the Cauchy problem for models of large amplitude internal waves, Nonlinearity **23**, 237 (2010).

[36] V. E. Zakharov, Stability of periodic waves of finite amplitude on the surface of a deep fluid, J. Appl. Mech. Tech. Phys. **9**, 190 (1968).

[37] P. Guyenne, Envelope equations for three-dimensional gravity and flexural-gravity waves based on a Hamiltonian approach, Fields Inst. Commun. **75**, 135 (2015).

[38] P. Guyenne and E. I. Părău, *Proceedings of the 25th International Ocean and Polar Engineering Conference, Kona, 2015* (ISOPE, Cupertino, 2015), pp. 467–475.

[39] M. S. Longuet-Higgins and E. D. Cokelet, The deformation of steep surface waves on water I. A numerical method of computation, Proc. R. Soc. London Ser. A **350**, 1 (1976).

[40] A. Clément, Coupling of two absorbing boundary conditions for 2D time-domain simulations of free surface gravity waves, J. Comput. Phys. **126**, 139 (1996).

[41] T. D. Williams and V. A. Squire, Oblique scattering of plane flexural-gravity waves by heterogeneities in sea-ice, Proc. R. Soc. A **460**, 3469 (2004).

[42] P. Guyenne and D. P. Nicholls, A high-order spectral method for nonlinear water waves over moving bottom topography, SIAM J. Sci. Comput. **30**, 81 (2007).

[43] W. Craig, P. Guyenne, J. Hammack, D. Henderson, and C. Sulem, Solitary water wave interactions, Phys. Fluids **18**, 057106 (2006).

[44] L. Xu and P. Guyenne, Numerical simulation of three-dimensional nonlinear water waves, J. Comput. Phys. **228**, 8446 (2009).

[45] J.-M. Vanden-Broeck and F. Dias, Gravity-capillary solitary waves in water of infinite depth and related free-surface flows, J. Fluid Mech. **240**, 549 (1992).

[46] H. Michallet and F. Dias, Numerical study of generalized interfacial solitary waves, Phys. Fluids **11**, 1502 (1999).

[47] T. B. Benjamin, The stability of solitary waves, Proc. R. Soc. A **328**, 153 (1972).

[48] M. H. Meylan, L. G. Bennetts, and A. L. Kohout, In-situ measurements and analysis of ocean waves in the Antarctic marginal ice zone, Geophys. Res. Lett. **41**, 5046 (2014).

[49] M. J. Doble, G. De Carolis, M. H. Meylan, J.-R. Bidlot, and P. Wadhams, Relating wave attenuation to pancake ice thickness, using field measurements and model results, Geophys. Rev. Lett. **42**, 4473 (2015).

[50] E. Părău and J.-M. Vanden-Broeck, Three-dimensional waves beneath an ice sheet due to a steadily moving pressure, Philos. Trans. R. Soc. A **369**, 2973 (2011).